INORGANIC CHEMISTRY FRONTIERS

RESEARCH ARTICLE

View Article Online
View Journal | View Issue

Cite this: *Inorg. Chem. Front.*, 2024, **11**, 6898

Thermally stable NIR broad emission of Cr^{3+} doping phosphor with a high output power†

Zhishan Chen,[d] Shaoan Zhang, *[b,c] Zhenzhang Li,[b] Huacong Ye,[d] Haoran Yan,[b] Jialong Xu,[d] Ling Gao,[a] Yang Li *[a,c,d] and Shizhen Zhang*[a]

The development of high-performance near-infrared (NIR) luminescent materials remains a significant challenge, particularly in enhancing thermal stability. Herein, we observed an anti-thermal quenching effect in the $YGa_{1.5}Al_{1.5}(BO_3)_4:Cr^{3+}$ phosphor, with its emission intensity reaching 104% at 423 K and 101% at 483 K compared to room temperature. This anti-thermal quenching is mainly attributed to thermal-induced emission compensation resulting from excited electrons trapped at crystal defects, as confirmed by density functional theory computation. Additionally, $YGa_{1.5}Al_{1.5}(BO_3)_4:Cr^{3+}$ exhibits a broad NIR emission peaking at 760 nm with a full width at half maximum of 135 nm and a high photoluminescence quantum yield (86%). As a proof-of-concept, we fabricated an NIR phosphor-converted light-emitting diode device that achieves an NIR output power of 59.67 mW with an input working current of 150 mA, demonstrating a photoelectric conversion efficiency of 13.6%. The utilization of this high-power NIR light-emitting diode device as a lighting source enables a penetration depth of up to 15 mm, demonstrating the potential applications of Cr^{3+}-doped $YGa_{1.5}Al_{1.5}(BO_3)_4:Cr^{3+}$ phosphors for non-invasive detection of biological tissue.

Received 9th July 2024,
Accepted 16th August 2024

DOI: 10.1039/d4qi01728e

rsc.li/frontiers-inorganic

1. Introduction

Integrating near-infrared (NIR) optical imaging technology into compact, portable smart devices and wearable optical gadgets has been an ongoing pursuit in recent years, aiming to achieve real-time monitoring of human health.[1–6] In the foreseeable future, silicon-based detectors integrated into smartphones will be extensively utilized for measuring oxygen content in blood, monitoring blood pressure, and detecting heart rate by leveraging the accuracy and user-friendliness of NIR technology.[2–4] While traditional NIR halogen lamps and semiconductor light-emitting diode (LED) arrays with their wide spectral range covering nearly the entire near-ultraviolet to NIR region face limitations such as high-power consumption, bulky size, and high operating temperature that restrict their application in miniaturized and portable devices.[5,6] In contrast to these traditional NIR sources, NIR phosphor-converted light-emitting diodes (pc-LEDs) exhibit more promising prospects due to their compact structure, long lifespan, low energy consumption, convenient lightweight design, especially with adjustable NIR spectrum distribution.[4–7] The rapid advancement in the research of NIR phosphors, activated by Cr^{3+} ions and regarded as ideal candidates, along with their efficient absorption of blue light, make them highly promising luminescent materials for applications in pc-LED devices.[8,9] However, the significant difference in energy between the excitation and emission spectra leads to a strong decrease in brightness for Cr^{3+}-doped NIR phosphors when exposed to high temperatures from blue LED chips.[10,11] Therefore, it is imperative to ensure optimal thermal stability while simultaneously ensuring high photoluminescence quantum efficiency.

As we know, the design of wideband NIR Cr^{3+}-activated phosphors poses a high-dimensional, multi-scale, and intricate scientific conundrum, wherein the performance of NIR Cr^{3+}-activated phosphors is not solely contingent upon the intrinsic properties of Cr^{3+} luminescent center but also intricately linked to the composition of elements, atomic arrangement, crystal structure, and particularly intertwined with the local structure of the luminescent center.[12–15] Henceforth, the selection of Cr^{3+} doped potential candidates assumes paramount significance. The double borates $RX_3(BO_3)_4$, where R

[a]*Department of Neurosurgery and Neurosurgical Disease Research Centre, The Second Affiliated Hospital of Guangzhou Medical University, Guangzhou, 510006, China. E-mail: zhangshizhen2024@yeah.net*
[b]*Institute of Light+X Science and Technology, Faculty of Electrical Engineering and Computer Science, Ningbo University, Ningbo, 315211, China. E-mail: zsagdut2016@yeah.net, lychris@sina.com*
[c]*School of Mathematics and Systems Science, Guangdong Polytechnic Normal University, Guangzhou, 510665, China*
[d]*School of Biomedical Engineering, Guangzhou Medical University, Guangzhou, 510006, China*

† Electronic supplementary information (ESI) available. See DOI: https://doi.org/10.1039/d4qi01728e

represents a rare earth ion and X denotes Al or Ga, exhibit heterogeneous isomorphism with the mineral huntite $CaMg_3(CO_3)_4$ and possess a layered structure comprising diverse sequences of Y- and Ga/Al-rich layers.[16,17] Adjacent [Ga/AlO_6] octahedra are interconnected through edges to form stable helical chains along the *c*-axis direction. These helical chains are linked with [YO_6] trigonal prisms and [BO_3] triangular planes by sharing bridging oxygen atoms, resulting in an exceptionally rigid and steadfast framework.[16,17] In addition to their remarkable structural rigidity, the unique structure of $YGa_{1.5}Al_{1.5}(BO_3)_4$, belonging to the $RX_3(BO_3)_4$ group, suggests its exceptional suitability for incorporating Cr^{3+} doping sites, positioning it as an outstanding candidate with great potential.

In our study, we conducted both experimental and theoretical calculations to investigate $YGa_{1.5}Al_{1.5}(BO_3)_4$:$Cr^{3+}$ phosphors. Moving on to experimental results, $YGa_{1.5}Al_{1.5}(BO_3)_4$:$Cr^{3+}$ exhibits a broad NIR emission with a peak at 760 nm and a full width at half maximum (FWHM) of 135 nm. Additionally, $YGa_{1.5}Al_{1.5}(BO_3)_4$:$Cr^{3+}$ demonstrated an impressive photoluminescence quantum yield (PLQY) of 86% and excellent thermal stability even at elevated temperatures (104% @423 K). The anti-thermal quenching observed in this study can be attributed to the defect level, which is caused by a coupling between the doped ion Cr^{3+} and the oxygen vacancy (V_O). To showcase its potential applications, we fabricated an NIR phosphor-converted LED device by coating our prepared $YGa_{1.5}Al_{1.5}(BO_3)_4$:$Cr^{3+}$ phosphors onto commercially available blue LED chips as a proof-of-concept demonstration. Remarkably, this LED device achieved significant NIR output power of up to 59.67 mW with an input working current of 150 mA while maintaining a remarkable photoelectric conversion efficiency of 13.6%. The utilization of this high-power NIR LED device as a lighting source enables a penetration depth of up to 15 mm, showcasing the potential applications of Cr^{3+}-doped $YGa_{1.5}Al_{1.5}(BO_3)_4$:$Cr^{3+}$ phosphors for non-invasive detection of biological tissue.

2. Experiments section

2.1. Synthesis

The $YGa_{1.5}Al_{1.5}(BO_3)_4$:$Cr^{3+}$ phosphor was synthesized using high-purity raw materials, including yttrium oxide (Y_2O_3, 99.99%), aluminum oxide (Al_2O_3, 99.99%), boron trioxide (B_2O_3, 99.95%), chromium(III) oxide (Cr_2O_3, 99.95%), and gallium oxide (Ga_2O_3, 99.99%) *via* the conventional solid-state reaction technique. Stoichiometric proportions of the precursors were measured based on the $YGa_{1.5}Al_{1.5}(BO_3)_4$:$Cr^{3+}$ composition with an additional 10 wt% boron trioxide to compensate for evaporation during the calcination process. The materials were thoroughly blended by milling in an agate mortar before transferring to a corundum crucible for further processing at a preheating stage of 500 °C for 2 hours in a muffle furnace followed by calcination at 1100 °C for 6 hours. After completion of the sintering process, the products were allowed to cool naturally to room temperature.

2.2. Measurements and characterizations

In this paper, the $YGa_{1.5}Al_{1.5}(BO_3)_4$:0.06$Cr^{3+}$ sample exhibited the highest PL intensity. Therefore, a doping concentration of 0.06 for Cr^{3+} was selected for the following experiment and characterization. The X-ray diffraction (XRD) patterns of the prepared Cr^{3+} doping phosphor were obtained using a Bruker D8 Advance X-ray diffractometer with Cu Kα1 radiation, operating at 40 kV and 20 mA. The photoluminescence (PL) and photoluminescence excitation (PLE) experiments were conducted using an FLS1000 fluorescence spectrophotometer (Edinburgh Instruments Ltd, UK). A 450 W ozone-free xenon was used as an excitation source for the steady-state measurements. Photoluminescence quantum efficiency (PLQY) of our prepared phosphors was measured on a quantum yields measurement system (C9920-02, Hamamatsu Photonics K.K., Japan). The high-temperature PL spectra of 300 K–600 K were measured by the Jobin Yvon Triax 320 fluorescence spectrometer equipped with a double excitation monochromator and a homemade high-temperature sample heater. The morphology and size of the particles were characterized by transmission electron microscope (TEM) with a FEI Talos F200S.

2.3. NIR LED fabrication

The NIR LEDs were created by utilizing the synthesized $YGa_{1.5}Al_{1.5}(BO_3)_4$:$Cr^{3+}$ NIR-emitting phosphor in combination with a blue LED from Shanghai Blu-ray Technology Co., Ltd, China. The epoxy resin to NIR phosphor mass ratio remained constant at 1 : 1. The electroluminescence spectrum (EL) of NIR LEDs was measured using a fiber spectrophotometer (Nova high-sensitivity spectrometer, Idea Optics, China). Output power and conversion efficiency were determined using an ATA 100 photoelectric measuring system (EVERFINE, China). Images were captured using an industrial night-vision camera (MVCA050-20GN, Hikvision, China). Meanwhile, the temperatures of the operating NIR LEDs were recorded with a thermal infrared camera (FOTRIC 280).

2.4. DFT calculations

In this investigation, we employed density functional theory (DFT) in conjunction with the projector-augmented wave (PAW) method as implemented in the Vienna *Ab initio* Simulation Package (VASP).[18] The Perdew–Burke–Ernzerhof (PBE) functional within the generalized gradient approximation (GGA) framework was utilized for exchange–correlation energy calculations.[19] The choice of the PBE functional is well-established for providing a good balance between computational efficiency and accuracy for a wide range of materials, including the types studied in this work.

To ensure computational accuracy, we initially validated the authenticity of the pseudopotentials used in our calculations. This involved comparing the calculated properties of well-known reference materials to experimental data and high-accuracy theoretical results. The basis functions of the PAW

method were defined with an energy cutoff of 550 eV, ensuring sufficient plane-wave basis set completeness for reliable results.[18,19]

For Brillouin zone sampling, we employed the Monkhorst–Pack method with a 5 × 5 × 5 *K*-point grid, providing a fine sampling mesh that ensures accurate integration over the reciprocal space. To achieve convergence of defect formation energies within a margin of ±0.2 eV, we carefully adjusted the supercell dimensions, *K*-point grids, and cutoff energies. This process included systematic testing and convergence studies to confirm that the chosen parameters yield reliable and accurate defect formation energies.

Additionally, the internal atomic positions within each supercell were allowed to relax until the forces exerted on the atoms were reduced below 0.01 eV $Å^{-1}$. This relaxation ensures that the structures are at their lowest energy configurations, which is critical for accurate defect energy calculations.

DFT calculations were performed to investigate the lattice occupancy of Cr^{3+} doping in $YGa_{1.5}Al_{1.5}(BO_3)_4$. The crystal structure data was obtained from the materials project database (no. mp-1216259, 40 atoms), where the lattice constants were determined as a = 5.9841 Å, b = 6.00002 Å, c = 11.3040 Å, α = 98.2333°, β = 98.0532°, and γ = 104.1277°, respectively. Initially, we optimized the structure of the supercell and obtained optimized lattice constants of a = 5.9825 Å, b = 6.0064 Å, c = 11.3200 Å, α = 98.2818°, β = 98.1212°, and γ = 104.0709°, which showed excellent agreement with results from the crystal library analysis. After performing optimization, the monomer cell was expanded to create a supercell with dimensions of 2 × 2 × 1, containing a total of 160 atoms. The coordination and atomic radii (R_{Cr} = 1.18 Å, R_{Al} = 1.18 Å, R_{Ga} = 1.26 Å, R_Y = 1.62 Å) imply the potential for substitution of Al and Ga sites with Cr^{3+} ions in the $YGa_{1.5}Al_{1.5}(BO_3)_4$ crystal lattice. Thus, an analysis was conducted on the distribution of Cr^{3+} on various sites within the supercell: specifically, the Al site (Cr–Al), Ga site (Cr–Ga), and Y site (Cr–Y). Considering that Al and Ga have similar local structures within the crystal lattice, simultaneous occupation of Cr on both Al and Ga systems (Cr–Al/Ga) was analyzed. Initially, we optimized the structure of the doped system within the supercell followed by computation of its corresponding formation energy:[20,21]

$$E_f = E_D - E_H + \sum_i w_i n_i u_i$$

where E_f (X) represents the formation energy for the stable configuration denoted by X, while E_D (X) represents the aggregate energy of the said stable configuration X. Additionally, E_H corresponds to the aggregate energy of the stable $YGa_{1.5}Al_{1.5}(BO_3)_4$ structure. The variable w assumes a value of −1 when an atom i is incorporated, and conversely, it takes a value of 1 when an atom i is extracted. The variable n_i represents the number of atoms i. In this scenario, the chemical potential of the i atoms, represented as μ_i, is computed by employing the subsequent methodology.

The chemical potentials for B (u_B), Y (u_Y), Al (u_{Al}), Ga (u_{Ga}), and Cr (u_{Cr}) are obtained from their respective bulk metallic phases. The baseline energy for an oxygen molecule is expressed as u_O, which is defined as half of the total energy for a single O_2 molecule ($u_O = 1/2u_{O_2}$). When undergoing processes deviating from equilibrium, it is crucial to ensure that the chemical potential for any given atom does not exceed its elemental ground state chemical potential. Additionally, the formation energy (Δ) of the stable phase $YGa_{1.5}Al_{1.5}(BO_3)_4$ is characterized by a negative value, indicating that $\Delta = E_H(YGa_{1.5}Al_{1.5}(BO_3)_4) - u_Y\,(\text{bulk}) - 1.5u_{Ga}\,(\text{bulk}) - 1.5u_{Al}\,(\text{bulk}) - 4u_B\,(\text{bulk}) - 12u_O < 0$. In this framework, we equate u_O in its gaseous state to u_O in the solid state. Hence, the determined values for u_Y, u_{Al}, u_{Ga}, u_B, and u_O must comply with the following conditions:[20,21]

$$\Delta + u_Y\,(\text{bulk}) \le u_Y \le u_Y\,(\text{bulk}),$$

$$\Delta + 1.5u_{Ga}\,(\text{bulk}) \le 1.5u_{Ga} \le 1.5u_{Ga}\,(\text{bulk}),$$

$$\Delta + 1.5u_{Al}\,(\text{bulk}) \le 1.5u_{Al} \le 1.5u_{Al}\,(\text{bulk}),$$

$$\Delta + 4u_B\,(\text{bulk}) \le 4u_B \le 4u_B\,(\text{bulk}),$$

$$\Delta + 12u_O\,(\text{gas}) \le 12u_O \le 12u_O\,(\text{gas}).$$

3. Results and discussion

3.1. XRD refinements and crystal structure

To investigate the impact of Cr^{3+} doping concentration on the crystal structure, Fig. 1a presents the XRD patterns of as-prepared $YGa_{1.5}Al_{1.5}(BO_3)_4$:$xCr^{3+}$ (x = 0.02, 0.04, 0.06, and 0.08) samples. The diffraction peaks in Fig. 1a exhibit excellent agreement with the standard card ISCD no. 91963, indicating the incorporation of Cr^{3+} into the $YGa_{1.5}Al_{1.5}(BO_3)_4$ host due to their similar ionic radii with Ga^{3+}/Al^{3+}.[11,17] The main diffraction peak at 33° in Fig. 1a exhibits a blue shift, indicating the influence of Cr^{3+} on the crystal structure of the $YGa_{1.5}Al_{1.5}(BO_3)_4$ host. To gain insights into the effect of Cr^{3+} substitution on the crystal structure of $YGa_{1.5}Al_{1.5}(BO_3)_4$, the *Rietveld* refinement results were performed on both $YGa_{1.5}Al_{1.5}(BO_3)_4$ host and $YGa_{1.5}Al_{1.5}(BO_3)_4$:0.06$Cr^{3+}$ sample. The crystal structure of $YGa_{1.5}Al_{1.5}(BO_3)_4$ was initially chosen as a model for structural refinements. Fig. 1b and c display the experimental, calculated, and difference patterns of $YGa_{1.5}Al_{1.5}(BO_3)_4$ host and $YGa_{1.5}Al_{1.5}(BO_3)_4$:0.06$Cr^{3+}$ sample, respectively. The structural refinements, including space group, unit cell parameters and R factors, for both $YGa_{1.5}Al_{1.5}(BO_3)_4$ host and $YGa_{1.5}Al_{1.5}(BO_3)_4$:0.06$Cr^{3+}$ sample are presented (Table S1†). Low R factors indicate an excellent fit between experimental and calculated XRD patterns. Based on crystallographic parameters of $YGa_{1.5}Al_{1.5}(BO_3)_4$ host, the corresponding crystal structure was constructed. Furthermore, the atomic coordinate parameters of $YGa_{1.5}Al_{1.5}(BO_3)_4$ host and $YGa_{1.5}Al_{1.5}(BO_3)_4$:0.06$Cr^{3+}$ sample are presented in Table S2.†

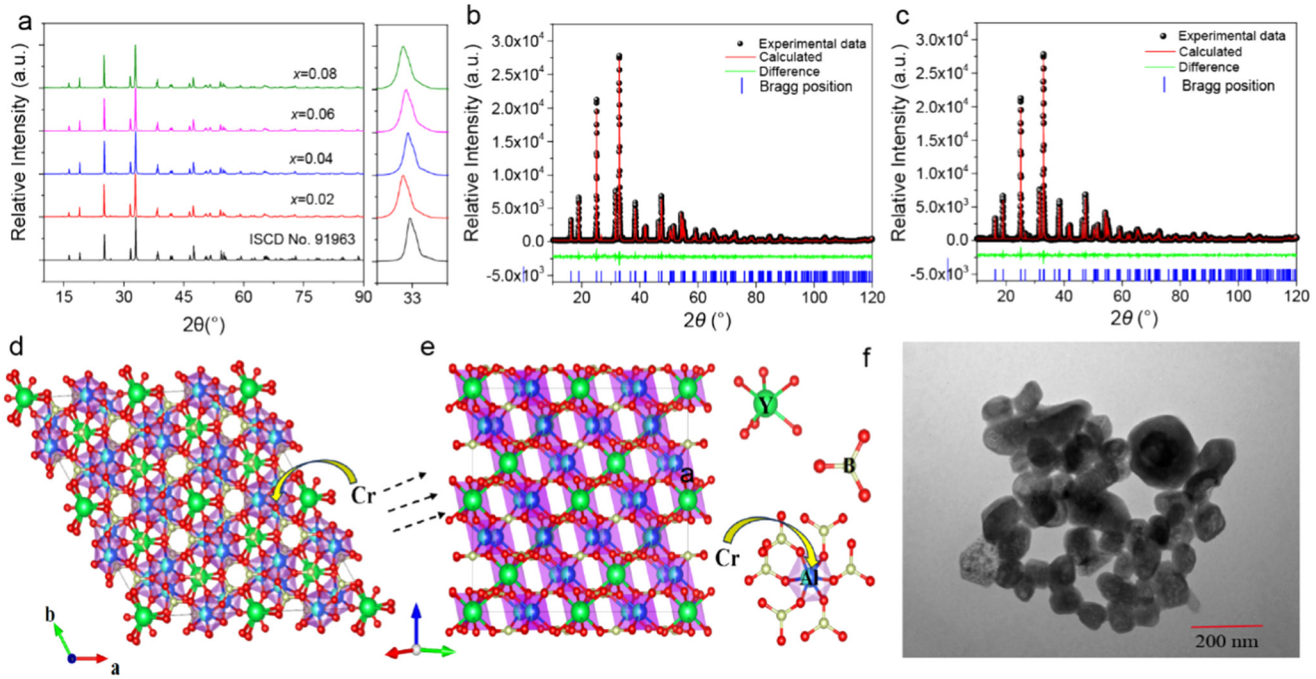

Fig. 1 (a) XRD patterns of as-prepared $YGa_{1.5}Al_{1.5}(BO_3)_4$:$xCr^{3+}$ (x = 0.02, 0.04, 0.06, and 0.08) samples; (b and c) *Rietveld* refinement results of $YGa_{1.5}Al_{1.5}(BO_3)_4$ host and $YGa_{1.5}Al_{1.5}(BO_3)_4$:$0.06Cr^{3+}$ sample, respectively; (d and e) crystal structure of $YGa_{1.5}Al_{1.5}(BO_3)_4$ host and $YGa_{1.5}Al_{1.5}(BO_3)_4$:$0.06Cr^{3+}$ sample along with the YO_6, Ga/AlO_6 and BO_3 polyhedron; (f) TEM of $YGa_{1.5}Al_{1.5}(BO_3)_4$:$0.06Cr^{3+}$ sample.

As shown in Fig. 1d, the crystal structure of $YGa_{1.5}Al_{1.5}(BO_3)_4$ host consists of three polyhedral YO_6, Ga/AlO_6 and BO_3. The unique feature of $YGa_{1.5}Al_{1.5}(BO_3)_4$ host can be characterized as a framework layer, which is formed by two Ga/AlO_6 octahedra sharing corners (Fig. 1e). Notably, Ga/Al ions are situated in a distorted octahedral coordination environment, potentially enhancing the optical absorption intensity of Cr^{3+} ions when Cr^{3+} substitutes for the Ga/Al site. In Fig. 1f, TEM analysis reveals that the particle size measures approximately 200 nm, exhibiting excellent dispersion characteristics.

3.2. Photoluminescence performance

As illustrated in Fig. 2a, $YGa_{1.5}Al_{1.5}(BO_3)_4$ host exhibits a high diffuse reflectance within the visible region, spanning 350 to 800 nm; however, there is a significant reduction within the ultraviolet (UV) region (200–300 nm), which is ascribed to the bandgap absorption of $YGa_{1.5}Al_{1.5}(BO_3)_4$ host. $YGa_{1.5}Al_{1.5}(BO_3)_4$:$0.06Cr^{3+}$ sample exhibits two broad absorption bands at 430 and 600 nm, arising from the ground state $^4A_{2g}$ to $^4T_{1g}$ and $^4T_{2g}$ of Cr^{3+} ions, respectively. The bandgap of the $YGa_{1.5}Al_{1.5}(BO_3)_4$ host can be determined by analyzing the UV absorption edge. Assuming the $YGa_{1.5}Al_{1.5}(BO_3)_4$ host to be a direct bandgap material, the corresponding optical bandgap (E_g) was estimated using the following equation:[22,23]

$$(\alpha h\nu)^2 = A(h\nu - E_g) \quad (1)$$

where A is a constant related to the properties of the bands, and $h\nu$ is the photon energy. According to Kubelka–Munk theory, the absorption coefficient (α) in Eq. (1) can be substituted with $F(R_\infty)$:[22,23]

$$F(R_\infty) = \frac{(1-R_\infty)^2}{2R_\infty} \quad (2)$$

The reflectance of $YGa_{1.5}Al_{1.5}(BO_3)_4$ host is denoted as R_∞. The Tauc plot in Fig. 2b illustrates the optical bandgap of approximately 4.6 eV for the $YGa_{1.5}Al_{1.5}(BO_3)_4$ host.

In Fig. 2c, a broad band between 350–500 nm results from the transition of Cr^{3+} from the ground state $^4A_{2g}$ to the first excited state $^4T_{2g}$, while another broad band centered at 611 nm is ascribed to the $^4A_{2g} \rightarrow {}^4T_{1g}$ transition of Cr^{3+} ions.[24,25] It is worth noting that the FWHM of the PLE broad bands at 430 nm is calculated to be 81 nm, with a wide FWHM being suitable for the stimulation of commercial blue LED chips. Under 430 nm blue light stimulation, Fig. 2c shows a broad NIR emission extending from the red to the NIR region (625–850 nm), which originates from the $^4T_{2g}$ (4F) $\rightarrow {}^4A_{2g}$ (4F) transition of Cr^{3+} with a FWHM as wide as 135 nm. A line emission at 683 nm is attributed to the spin-forbidden $^2E_g \rightarrow {}^4A_{2g}$ transitions (R-lines) of Cr^{3+}.[24,25] PL intensity of $YGa_{1.5}Al_{1.5}(BO_3)_4$:$Cr^{3+}$ in Fig. 2d exhibits a dependence on the doping concentration of Cr^{3+}, with the optimal value observed at a doping concentration of 0.06 for Cr^{3+}. The presence of both $^2E \rightarrow {}^4A_2$ transitions and $^4T_{2g}$ (4F) $\rightarrow {}^4A_{2g}$ (4F) of Cr^{3+} indicates the existence of an intermediate crystal field.[1,26,27] Whether the emission from Cr^{3+} is broadband or a sharp line depends on the interaction between Cr^{3+} and its surrounding ligands, which can be evaluated by crystal field strength D_q as

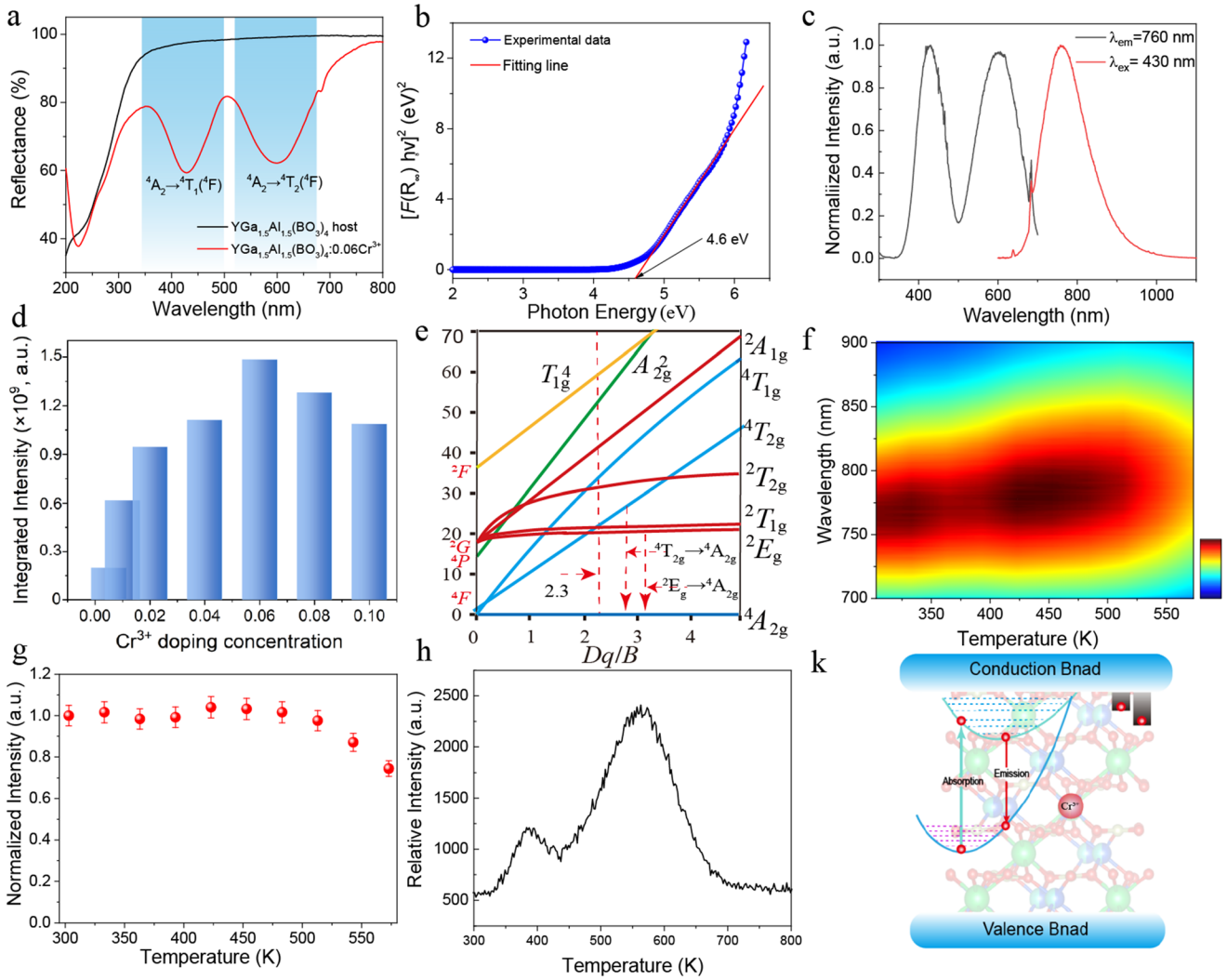

Fig. 2 (a) Reflectance spectra of $YGa_{1.5}Al_{1.5}(BO_3)_4$ host and $YGa_{1.5}Al_{1.5}(BO_3)_4$:0.06$Cr^{3+}$ sample; (b) the corresponding bandgap; (c) PLE and PL spectra of $YGa_{1.5}Al_{1.5}(BO_3)_4$:0.06$Cr^{3+}$ sample; (d) PL intensity of $YGa_{1.5}Al_{1.5}(BO_3)_4$:$Cr^{3+}$ with different Cr^{3+} doping concentrations; (e) Tanabe–Sugano diagram for Cr^{3+} in an octahedral site; (f) the temperature-dependent PL spectrum and (g) integrated intensity of $YGa_{1.5}Al_{1.5}(BO_3)_4$:0.06$Cr^{3+}$ sample ranging from room temperature to 583 K; (h) thermoluminescence spectrum of $YGa_{1.5}Al_{1.5}(BO_3)_4$:0.06$Cr^{3+}$ sample under the blue light irradiation for 5 min; (k) mechanism diagram of anti-thermal quenching behavior for $YGa_{1.5}Al_{1.5}(BO_3)_4$:$Cr^{3+}$ sample.

well as two Racah parameters B and C. The values of D_q, B, and C parameters were calculated by the following equations:[28,29]

$$10D_q = E(^4A_{2g} - {}^4T_{2g}) - \Delta S/2 \quad (3)$$

$$\frac{D_q}{B} = \frac{15(\Delta E/D_q - 8)}{(\Delta E/D_q)^2 - 10(\Delta E/D_q)} \quad (4)$$

$$\Delta E = E(^4A_{2g} \rightarrow {}^4T_{1g}) - E(^4A_{2g} \rightarrow {}^4T_{2g}) \quad (5)$$

where ΔE represents the central wavenumber difference of the $^4T_{2g}$ and $^4T_{1g}$ states which depends on the excitation position of $^4A_{2g} \rightarrow {}^4T_{2g}$ and $^4A_{2g} \rightarrow {}^4T_{1g}$ transitions in PLE spectrum and ΔS is the stokes-shift. Considering $E(^4A_{2g} \rightarrow {}^4T_{2g})$ = 16528 cm^{-1} and $E(^4A_{2g} \rightarrow {}^4T_{1g})$ = 23255 cm^{-1}, the values of D_q, and B parameters were calculated to be 1316, and 731 cm^{-1}, respectively. Based on those above parameters, the D_q/B value was calculated to be 1.80, which is much lower than that of the crossover point ($D_q/B \approx 2.3$) between $^4A_{2g}$ and ^2E excited states, as shown in Fig. 2e.[30] These results indicate that the ^2E_g state locates lower than the $^4T_{2g}$ state in energy, resulting in the narrow line emission from the ^2E_g and the broadband emission from the $^4T_{2g}$ excited state of Cr^{3+} in $YGa_{1.5}Al_{1.5}(BO_3)_4$.

Fig. 2f and g show the temperature-dependent PL spectrum and integrated intensity of $YGa_{1.5}Al_{1.5}(BO_3)_4$:0.06$Cr^{3+}$ sample ranging from room temperature to 573 K. The PL intensity of $YGa_{1.5}Al_{1.5}(BO_3)_4$:0.06$Cr^{3+}$ sample in Fig. 2g reached its maximum value (104%) at 423 K, and 101% at 483 K compared to that at room temperature, and subsequently declined to 74.4% of room temperature as the temperature rose to 573 K. The anti-thermal quenching of Cr^{3+} in $YGa_{1.5}Al_{1.5}(BO_3)_4$ can be

attributed to the rigid structure of the host material, $YGa_{1.5}Al_{1.5}(BO_3)_4$, on one hand, and to the trapping of excited electrons at trap defects on the other (Fig. 2h). In Fig. 2h, the thermoluminescence (TL) spectrum confirmed the existence of trap defects in the $YGa_{1.5}Al_{1.5}(BO_3)_4$:0.06$Cr^{3+}$ sample. Based on the empirical equation $E_{trap} = T/500$ eV, the trap depth (E_{trap}) was estimated at 0.78 and 1.16 eV, which might be attributed to trap levels.[31–33] The anti-thermal quenching behavior of $YGa_{1.5}Al_{1.5}(BO_3)_4$:$Cr^{3+}$ sample can be explained as follows: when the electrons on the $^4T_{2g}$ ground state of Cr^{3+} ions are excited to the $^4A_{2g}$ excited state, they undergo two competitive processes: radiative emission and non-radiative cross-relaxation, thermal ionization or energy transfer to quenching centers. At elevated temperatures, the non-radiative probability increases leading to the thermal quenching in PL intensity.[34–36] However, electrons released thermally from trap levels and recombined by the Cr^{3+}–$^4A_{2g}$ state compensate for this loss at high temperatures, resulting in dynamic equilibrium between non-radiative and recombination processes that achieve anti-thermal quenching behavior.[37,38] In the following, we will discuss in detail the attribution of defect levels through DFT.

3.3. DFT calculations of $YGa_{1.5}Al_{1.5}(BO_3)_4$:$Cr^{3+}$

Based on DFT calculations, the formation energies of Cr–Al, Cr–Ga, Cr–Al/Ga, and Cr–Y are determined to be −2.39 eV, −3.46 eV, −3.06 eV, and 5.99 eV, respectively. It is evident that the formation energy of Cr–Al is comparatively low, indicating a strong preference for Cr^{3+} to occupy the Al^{3+} site within the crystal lattice. Furthermore, these findings suggest a pronounced affinity between Cr^{3+} and Al^{3+} atoms in this specific crystal structure due to their similar atomic radii and coordi-

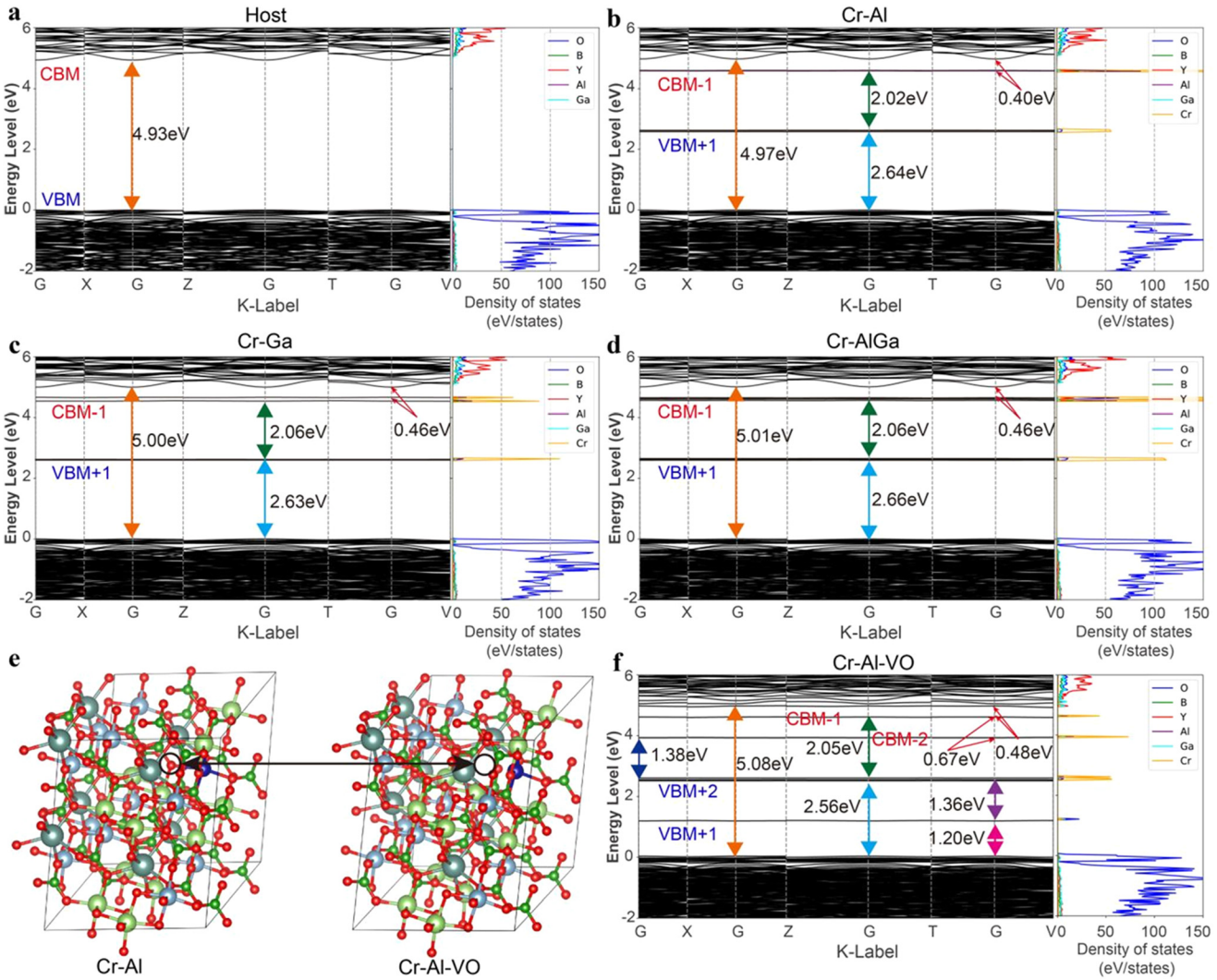

Fig. 3 Calculated band and density-of-states structure of (a) $YGa_{1.5}Al_{1.5}(BO_3)_4$, (b) Cr–Al, (c) Cr–Ga, (d) Cr–Al/Ga and (f) Cr–Al–V_O, which represents the perfect system, the case system where Cr^{3+} occupies Al^{3+}, the case system where Cr^{3+} occupies Ga^{3+}, the case system where Cr^{3+} occupies both Al^{3+} and Ga^{3+}, and the oxygen vacancy system, respectively; (e) crystal structure of Cr–Al sample (left) and Cr–Al sample with a neighboring oxygen defect (V_O).

nation environments which facilitate their mutual incorporation into the lattice. However, upon considering both the Cr–Ga and Cr–Al/Ga systems, it becomes evident that their formation energies closely resemble that of Cr–Al, implying a potential coexistence within the crystal structure.[39–41]

The impact of Cr^{3+} on the bandgap and density-of-states (DOS) of the $YGa_{1.5}Al_{1.5}(BO_3)_4$ host was investigated through DFT calculations. As shown in Fig. 3a, the $YGa_{1.5}Al_{1.5}(BO_3)_4$ host exhibits a direct band gap of 4.93 eV. It is noteworthy that the conduct band (CB) primarily consists of DOS contributed by Y atoms, and the valence band (VB) mainly comprises DOS from O atoms. In Fig. 3b–d, there is a significant influence on the band gap, with calculated values of 4.97 eV, 5.00 eV, and 5.01 eV for Cr^{3+} ions occupying Al, Ga or Al/Ga sites, respectively. Furthermore, the introduction of Cr^{3+} ions in Fig. 3b–d results in one defect level of 2.64 eV, 2.63 eV and 2.66 eV above VB maximum (VBM + 1), while the other defect level of 0.40 eV, 0.46 eV and 0.46 eV below CB minimum (CBM − 1), respectively; this phenomenon can be attributed to explain the energy level transition of Cr^{3+} in $YGa_{1.5}Al_{1.5}(BO_3)_4$.[42–45]

The doped lattice structure of Cr^{3+} generally exhibits a propensity for oxygen vacancy defects, which in turn play a crucial

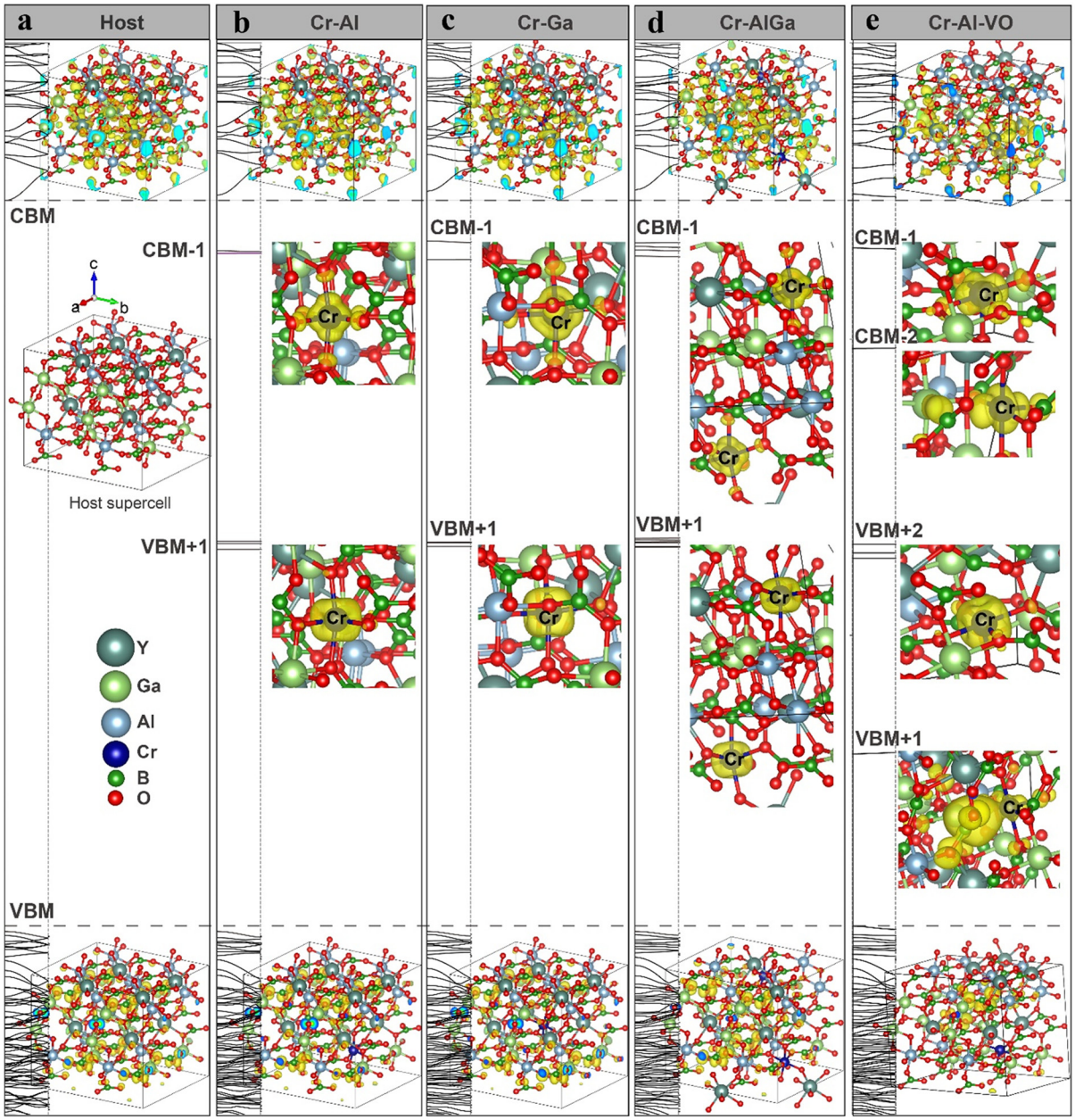

Fig. 4 Calculated charge density of (a) $YGa_{1.5}Al_{1.5}(BO_3)_4$ host, (b) Cr–Al, (c) Cr–Ga and (d) Cr–Al/Ga, and (e) Cr–Al–V_O, which represents the perfect system, the case system where Cr^{3+} occupies Al^{3+}, the case system where Cr^{3+} occupies Ga^{3+}, the case system where Cr^{3+} occupies both Al^{3+} and Ga^{3+}, and Cr–Al with the oxygen vacancy system, respectively.

role in the formation of trap levels. Therefore, to delve deeper into the specific mechanism underlying trap level formation, we will simulate the scenario where Cr^{3+} occupies the Al^{3+} lattice and experiences localized structural oxygen loss, as this closely resembles real-world conditions (Fig. 3e). In Fig. 3f, when oxygen defects (V_O) form at the doping position, there is an increase in the band gap (5.08 eV), resulting in two new energy levels located at 1.20 eV above VBM (VBM + 1) and at 2.05 eV below CBM (CBM + 2). VBM + 1 primarily arises from the coupling between Cr^{3+} and V_O, while CBM + 2 mainly originates from Cr atoms due to electron or hole release when Cr–O bonds break. The other two energy levels (CBM − 1 and VBM + 2) exhibit similarities with those of the Cr–Al system (CBM − 1 and VBM + 1). Therefore, we can conclude that the attribution of the defect level that determines the thermal stability of Cr^{3+} is not only caused by the oxygen vacancy but also by the coupling of the doped ion Cr^{3+} and the V_O.

Compared with Fig. 4a, introducing Cr^{3+} into the Al^{3+} sites in Fig. 4b significantly disturbs the band structure and electronic structures, leading to alteration in the depth of defect levels at the VBM due to variations in its DOS curve shape while still maintaining dominance in composition within VBM's oxygen orbital component. This can be attributed to substituting Cr^{3+} ions in octahedral Al^{3+} sites, which impacts the electronic orbital distribution of O atoms near the original Al lattice site. The CBM is minimally affected and remains composed of Y, Ga, B, and O. The defect energy levels of VBM + 1 and VBM + 2 primarily result from Cr doping, with electron orbitals mainly consisting of Cr along with minor amounts of O, B, and Y components. However, the DOS of CBM − 1 is significantly higher than that of VBM + 1.

When both Al and Ga are occupied by Cr^{3+} (Fig. 4d), the energy levels of the VBM and CBM exhibit a remarkable similarity to those of Al. In the defect level within the band gap, VBM + 1 exhibits a morphology highly resembling that of the Cr–Al system (Fig. 4b), while CBM − 1 displays a morphology similar to that of the Cr–Ga system. Notably, CBM − 1 possesses a higher charge density compared to VBM + 1. The dominant similarity lies in the components related to Cr^{3+}, whereas the O, B, and Y components demonstrate relatively

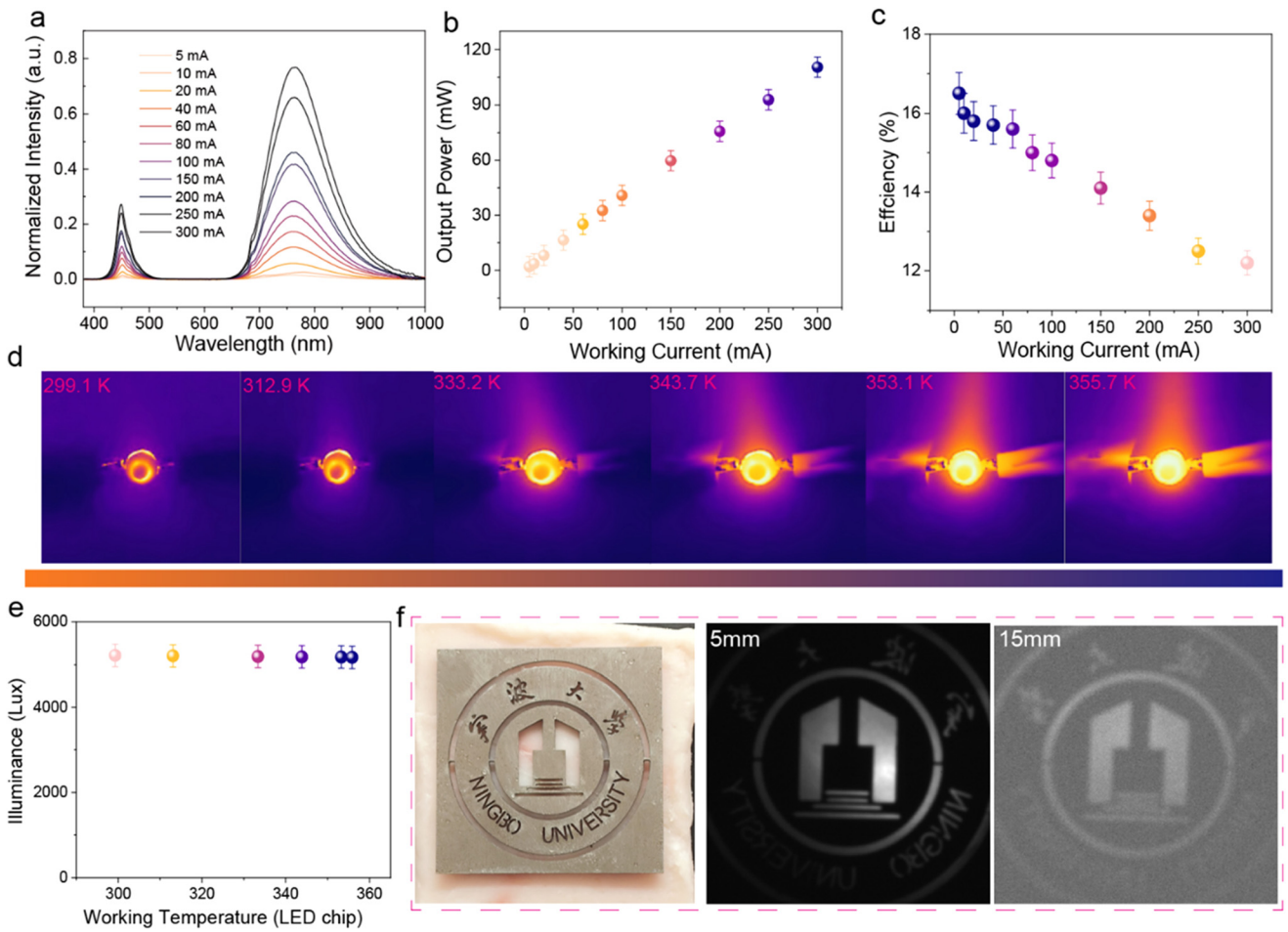

Fig. 5 (a) Driven current-dependent electroluminescence spectra of the fabricated NIR LED; (b) output optical power of NIR pc-LEDs depending on the working current; (c) conversion photoelectric efficiency of NIR pc-LEDs depending on the working current; (d) thermographs of the NIR pc-LEDs device at different driven currents; (e) dependence of the electroluminescence intensity of NIR pc-LEDs on the working electric current; (f) depth of penetration of NIR LED to biological tissue.

minor similarities. When Cr^{3+} simultaneously occupies the Al and Ga sites, the charge density of the resulting energy level is comparable to that of Cr–Ga or Cr–AI, with the exception that the charge density of Cr^{3+} increases. This can be interpreted as a superposition of the charge coupling between Cr–Ga and Cr–AI. In the presence of an oxygen vacancy near the Cr–AI system, significant disturbances occur in both O and Ga atoms due to the breakage of Cr–O bonds.[45,46] Consequently, a new energy level VBM + 1 is predominantly formed by disturbances from Cr, Ga, and O; while CBM + 2 is primarily influenced by disturbances from Cr and O. The electron cloud states for VBM + 2 and CBM + 1 resemble those observed in Cr–Ga or Cr–AI systems (Fig. 4e).

3.4. NIR performance of LED chips

The electroluminescence (EL) spectra of the NIR pc-LED device, fabricated by coating $YGa_{1.5}Al_{1.5}(BO_3)_4$:$Cr^{3+}$ NIR phosphors onto a commercial blue LED chip, are presented in Fig. 5a. As depicted in Fig. 5a, the electroluminescence intensity of our NIR pc-LEDs exhibits an upward trend with increasing working current. Fig. 5b and c show the output optical power and conversion photoelectric efficiency of the NIR pc-LEDs, respectively. Notably, the output power surged from 40.8 mW at 100 mA to an impressive 59.67 mW at 150 mA (Fig. 5b). Furthermore, when operated at high currents up to 100 mA and 150 mA in Fig. 5c, the exceptional NIR pc-LED chip demonstrates a commendable conversion photoelectric efficiency of 10.9% and 13.6%, respectively as depicted in Table S3.†

The real-time temperature rise of LED devices under maximum operating current was continuously monitored to ensure their long-term stability, as shown in Fig. 5d. The dependence of EL intensity on working temperature for LED devices driven at a current of 300 mA. After three hours of uninterrupted operation under this maximum current (300 mA), the working temperature reached its peak value at approximately 355.7 K. However, due to the outstanding thermal stability exhibited by $YGa_{1.5}Al_{1.5}(BO_3)_4$:$Cr^{3+}$, only a marginal five percent decrease in EL intensity was observed for the LED device (Fig. 5e). The utilization of NIR pc-LED offers significant advantages due to its exceptional tissue penetration capability without causing any harm or discomfort to the individual. As depicted in Fig. 5f, by employing this high-power NIR LED device, it becomes feasible to achieve an impressive depth of pork tissue penetration up to 15 mm, thereby emphasizing the vast potential applications of Cr^{3+}-doped $YGa_{1.5}Al_{1.5}(BO_3)_4$:$Cr^{3+}$ phosphors for non-invasive detection of biological tissue.[43,46]

4. Conclusions

In this paper, the $YGa_{1.5}Al_{1.5}(BO_3)_4$ host is a direct band gap material with a band gap of 4.93 eV. In comparison to other occupying sites, Cr^{3+} ions exhibit a preference for occupying Al sites due to their lower formation energy. Notably, the introduction of Cr^{3+} doping in Al sites results in the emergence of two defect levels near 2.64 eV (VBM + 1) and 0.40 eV (CBM − 1) within the band gap, which are closely associated with the luminescent properties exhibited by Cr^{3+}. Experimental results show that the $YGa_{1.5}Al_{1.5}(BO_3)_4$ host has an optical bandgap of approximately 4.6 eV, which is in agreement with the DFT calculation result. $YGa_{1.5}Al_{1.5}(BO_3)_4$:$Cr^{3+}$ exhibits a broad NIR emission peaking at 760 nm with a FWHM of 135 nm. Furthermore, $YGa_{1.5}Al_{1.5}(BO_3)_4$:$Cr^{3+}$ phosphors show a high PLQY (86%), and excellent thermal stability (104%@423 K and 101%@483 K). As a proof-concept demonstration, we fabricated an NIR phosphor-converted LED device by coating our prepared $YGa_{1.5}Al_{1.5}(BO_3)_4$:$Cr^{3+}$ phosphors onto commercial blue LED chips. This device achieves significant NIR output power up to 59.67 mW when the input working current reaches 150 mA, along with a remarkable photoelectric conversion efficiency of 13.6%. By utilizing this high-power NIR LED device, it becomes possible to achieve a remarkable penetration depth of up to 15 mm in biological tissue, thereby highlighting the immense potential applications of Cr^{3+}-doped $YGa_{1.5}Al_{1.5}(BO_3)_4$:$Cr^{3+}$ phosphors for non-invasive detection of biological tissue.

Data availability

The authors confirm that the data supporting the findings of this study are available within the article.

Conflicts of interest

There are no conflicts to declare.

Acknowledgements

This work is financially supported by the National Natural Science Foundation of China (Grant No. 52172083, 82203887), International Science & Technology Cooperation Program of Guangdong (Grant No. 2021A0505030078), and Guangzhou Key Research and Development Program (Grant No. 2023B03J1239), China Postdoctoral Science Foundation (No. 2022M720919) and Guangdong Basic and Applied Basic Research Foundation (No. 2021A1515110393, 2022A1515110463).

References

1 M. Zhang, P. Dang, Y. Wan, Y. Wang, Z. Zeng, D. Liu, Q. Zhang, G. Li and J. Lin, Tailoring Ultra-Wide Visible-NIR Luminescence by Ce^{3+}/Cr^{3+}/Yb^{3+}-alloying Sc-Based Oxides for Multifunctional Optical Applications, *Adv. Opt. Mater.*, 2024, **12**, 2302941.

2 Y. Wei, P. Dang, Z. Dai, G. Li and J. Lin, Advances in Near-Infrared Luminescent Materials without Cr^{3+}: Crystal Structure Design, Luminescence Properties, and Applications, *Chem. Mater.*, 2021, **33**, 5496–5526.

3 F. Y. Zhao, Z. Song and Q. L. Liu, Advances in Chromium-Activated Phosphors for Near-Infrared Light Sources, *Laser Photonics Rev.*, 2022, **16**, 2200380.
4 P. Dang, Y. Wei, D. Liu, G. Li and J. Lin, Recent Advances in Chromium-Doped Near-Infrared Luminescent Materials: Fundamentals, Optimization Strategies, and Applications, *Adv. Opt. Mater.*, 2022, **11**, 2201739.
5 G. N. A. De Guzman, M.-H. Fang, C.-H. Liang, Z. Bao, S.-F. Hu and R.-S. Liu, Near-infrared phosphors and their full potential: A review on practical applications and future perspectives, *J. Lumin.*, 2020, **219**, 116944.
6 M. D. Mehare, C. M. Mehare, H. C. Swart and S. J. Dhoble, Recent development in color tunable phosphors: A review, *Prog. Mater. Sci.*, 2023, **133**, 101067.
7 W. Yan, S. T. Chen, Y. X. Liu, Z. Y. Gao, Y. Wei and G. G. Li, Giant Photoluminescence Improvement and Controllable Emission Adjustment in Bi^{3+}-Activated $Ca_4Zr_3GeO_{12}$ Phosphors for High-Quality White Light-Emitting Diodes, *ACS Appl. Electron. Mater.*, 2019, **1**, 1970–1980.
8 Q. Zhang, X. Wei, J. Zhou, B. Milićević, L. Lin, J. Huo, J. Li, H. Ni and Z. Xia, Thermal Stability Improvement of Cr^{3+}-Activated Broadband Near-Infrared Phosphors via State Population Optimization, *Adv. Opt. Mater.*, 2023, **11**, 2300310.
9 A. Meijerink, Ultrabright near-infrared light, *Light: Sci. Appl.*, 2024, **13**, 73.
10 G. C. Liu, W. B. Chen, Z. Xiong, Y. Z. Wang, S. Zhang and Z. G. Xia, Laser-driven broadband near-infrared light source with watt-level output, *Nat. Photonics*, 2024, **18**, 562–568.
11 T. Wang, Y. Wang, W. Chen and Z. Xia, Crystallization of $Na_2SrGe_6O_{14}$:Cr^{3+},Yb^{3+} Glass Ceramics Enabling a Watt-Level Output Power NIR-I/NIR-II Lighting Source, *Laser Photonics Rev.*, 2023, **18**, 2300784.
12 M. Zhao, S. Liu, H. Cai, F. Zhao, Z. Song and Q. Liu, Efficient broadband near-infrared phosphor Sr_2ScSbO_6:Cr^{3+} for solar-like lighting, *Sci. China Mater.*, 2021, **65**, 748–756.
13 T. Liu, H. Cai, N. Mao, Z. Song and Q. Liu, Efficient near-infrared pyroxene phosphor $LiInGe_2O_6$:Cr^{3+} for NIR spectroscopy application, *J. Am. Ceram. Soc.*, 2021, **104**, 4577–4584.
14 G. G. Li, C. C. Lin, W. T. Chen, M. S. Molokeev, V. V. Atuchin, C. Y. Chiang, W. Z. Zhou, C. W. Wang, W. H. Li, H. S. Sheu, T. S. Chan, C. G. Ma and R. S. Liu, Photoluminescence Tuning via Cation Substitution in Oxonitridosilicate Phosphors: DFT Calculations, Different Site Occupations, and Luminescence Mechanisms, *Chem. Mater.*, 2014, **26**, 2991–3001.
15 C. Dou, C. X. Cai, Z. Song and Q. L. Liu, Highly Quantum Efficient and Thermally Stable Near-Infrared-Emitting K-β-Al_2O_3:Cr^{3+} Phosphor, *Adv. Opt. Mater.*, 2023, **12**, 2301579.
16 D. Santamaria-Perez, A. Otero-de-la-Roza, J. Ruiz-Fuertes, R. Chulia-Jordan, T. Marqueño, S. MacLeod and C. Popescu, Pressure and Temperature Effects on Low-Density $Mg_3Ca(CO_3)_4$ Huntite Carbonate, *J. Phys. Chem. C*, 2019, **124**, 1077–1087.
17 B. Malysa, A. Meijerink and T. Jüstel, Temperature dependent luminescence Cr^{3+}-doped $GdAl_3(BO_3)_4$ and $YAl_3(BO_3)_4$, *J. Lumin.*, 2016, **171**, 246–253.
18 G. Kresse and J. Furthmuller, Efficient iterative schemes for ab initio total-energy calculations using a plane-wave basis set, *Phys. Rev. B: Condens. Matter*, 1996, **54**, 11169–11186.
19 J. P. Perdew, K. Burke and M. Ernzerhof, Generalized Gradient Approximation Made Simple, *Phys. Rev. Lett.*, 1996, **77**, 3865–3868.
20 Z. Li, B. Zhong, Y. Cao, S. Zhang, Y. Lv, Z. Mu, Z. Hu and Y. Hu, Energy transfer and tunable luminescence properties in $Y_3Al_2Ga_3O_{12}$: Tb^{3+}, Eu^{3+} phosphors, *J. Alloys Compd.*, 2019, **787**, 672–682.
21 J. P. Perdew, A. Ruzsinszky, G. I. Csonka, O. A. Vydrov, G. E. Scuseria, L. A. Constantin, X. L. Zhou and K. Burke, Restoring the density-gradient expansion for exchange in solids and surfaces, *Phys. Rev. Lett.*, 2008, **100**, 136406.
22 W. Xiao, E. T. Basore, G. Zheng, X. Liu, B. Xu and J. Qiu, Suppressed Concentration Quenching Brightens Short-Wave Infrared Emitters, *Adv. Mater.*, 2023, **35**, e2306517.
23 E. T. Basore, W. G. Xiao, X. F. Liu, J. H. Wu and J. R. Qiu, Broadband Near-Infrared Garnet Phosphors with Near-Unity Internal Quantum Efficiency, *Adv. Opt. Mater.*, 2020, **8**, 2000296.
24 V. Rajendran, W. T. Huang, K. C. Chen, H. Chang and R. S. Liu, Energy-saving chromium-activated garnet-structured phosphor-converted near-infrared light-emitting diodes, *J. Mater. Chem. C*, 2022, **10**, 14367–14378.
25 G. N. A. De Guzman, S. F. Hu and R. S. Liu, Enticing applications of near-infrared phosphors: Review and future perspectives, *J. Chin. Chem. Soc.*, 2020, **68**, 206–215.
26 W. T. Huang, K. C. Chen, M. H. Huang and R. S. Liu, Tunable Spinel Structure Phosphors: Dynamic Change in Near-Infrared Windows and Their Applications, *Adv. Opt. Mater.*, 2023, **11**, 2301166.
27 M. H. Chan, W. T. Huang, K. C. Chen, T. Y. Su, Y. C. Chan, M. Hsiao and R. S. Liu, The optical research progress of nanophosphors composed of transition elements in the fourth period of near-infrared windows I and II for deep-tissue theranostics, *Nanoscale*, 2022, **14**, 7123–7136.
28 Y. Tanabe and S. Sugano, On the absorption spectra of complex ions II, *J. Phys. Soc. Jpn.*, 1954, **9**, 766–779.
29 A. Trueba, P. Garcia-Fernandez, J. M. García-Lastra, J. A. Aramburu, M. T. Barriuso and M. Moreno, A Cr^{3+}-Doped Fluorides and Oxides: Role of Internal Fields and Limitations of the Tanabe-Sugano Approach, *J. Phys. Chem. A*, 2011, **115**, 1423.
30 S. Xu, J. Feng, D. Zhang, B. Zhang, D. Wen, M. Wu and J. Li, Quantifying rigidity for thermally stable Cr^{3+} phosphors, *Phys. Chem. Chem. Phys.*, 2023, **25**, 29303–29309.
31 F. Zhu, Y. Gao, C. Zhao, J. Pi and J. Qiu, Achieving Broadband NIR-I to NIR-II Emission in an All-Inorganic Halide Double-Perovskite Cs_2NaYCl_6:Cr^{3+} Phosphor for Night Vision Imaging, *ACS Appl. Mater. Interfaces*, 2023, **15**, 39550–39558.

32 C. Zhang, L. Huang, J. Wang, T. Zhou and R.-J. Xie, Screening of Broadband Near-Infrared Cr^{3+}-Activated Phosphors Using Ce^{3+} as a Probe, *Chem. Mater.*, 2023, **35**, 2038–2046.

33 P. Luo, D. Sun, Z. Lyu, S. Wei, Z. Lu, L. Zhou, X. Zhang, S. Shen and H. You, Remote Control and Noninvasive Detection Enabled by a High-performance NIR pc-LED, *Inorg. Chem.*, 2024, **63**, 2655–2662.

34 S. Saikia, A. Ghosh and A. Nag, Broad Dual Emission by Codoping Cr^{3+} (d→d) and Bi^{3+} (s→p) in $Cs_2Ag_{0.6}Na_{0.4}$ $InCl_6$ Double Perovskite, *Angew. Chem., Int. Ed.*, 2023, **62**, e202307689.

35 Y. B. Ma, W. F. Liao, B. B. Quan, Z. H. Kong, M. S. Molokeev, A. Zolotov, M. Cheng, X. Y. Chen, Z. Zhou and M. Xia, Solid solution structural engineering enhances the luminescence of $SrMgAl_{10}O_{17}$:$Cr^{3+}$for agricultural lighting, *J. Lumin.*, 2024, **270**, 120553.

36 C. Wang, X. Zhang, C. Zhong, X. Wu, Y. Xu, S. Yin, Q. Yang, L. Zhou and H. You, Enhanced quantum efficiency and thermal stability by crystal-field engineering in a $Y(Ga, Al)_3(BO_3)_4$:Cr^{3+},Yb^{3+} phosphor for diverse short-wave infrared applications, *J. Mater. Chem. C*, 2024, **12**, 3515–3525.

37 Y. Wang, Y. Sun, Z. Xu, X. Xing and M. Shang, Two-Site Occupation for Constructing Double Perovskite $BaLaMgNbO_6$:Cr^{3+} Ultrabroadband NIR Phosphors, *Inorg. Chem.*, 2024, **63**, 8899–8907.

38 G. Chen, Y. Jin, L. Yuan, B. Wang, J. Huo, H. Suo, H. Wu, Y. Hu and F. Wang, Unlocking Cr^{3+}-Cr^{3+} Coupling in Spinel: Ultrabroadband Near-Infrared Emission beyond 900 nm with High Efficiency and Thermal Stability, *ACS Appl. Mater. Interfaces*, 2024, **16**, 30185–30195.

39 R. Li, Y. Liu, C. Jin, L. Zhang, J. Zhang, X. J. Wang, G. Chen and J. Jiang, Boosting Applications with High-Performance Near-Infrared Phosphor-Converted Light-Emitting Diodes, *Laser Photonics Rev.*, 2023, **18**, 2300608.

40 Z. Song, P. A. Tanner and Q. Liu, Host Dependency of Boundary between Strong and Weak Crystal Field Strength of Cr^{3+} Luminescence, *J. Phys. Chem. Lett.*, 2024, **15**, 2319–2324.

41 A. Balhara, S. K. Gupta, B. Modak, M. Abraham, A. K. Yadav, H. V. Annadata, S. Das, N. S. Rawat and K. Sudarshan, Synergy between structural rigidity and cluster defects in a bright near-infrared Cr^{3+}-based phosphor for excellent thermal stability and long afterglow, *J. Mater. Chem. C*, 2024, **12**, 9716–9732.

42 N. Majewska, Y. T. Tsai, X. Y. Zeng, M. H. Fang and S. Mahlik, Advancing Near-Infrared Light Sources: Enhancing Chromium Emission through Cation Substitution in Ultra-Broadband Near-Infrared Phosphors, *Chem. Mater.*, 2023, **35**, 10228–10237.

43 V. Rajendran, K. C. Chen, W. T. Huang, M. Kaminski, M. Grzegorczyk, S. Mahlik, G. Leniec, K. M. Lu, D. H. Wei, H. Chang and R. S. Liu, Unraveling Luminescent Energy Transfer Pathways: Futuristic Approach of Miniature Shortwave Infrared Light-Emitting Diode Design, *ACS Energy Lett.*, 2023, **8**, 2395–2400.

44 D. Liu, G. Li, P. Dang, Q. Zhang, Y. Wei, L. Qiu, H. Lian, M. Shang and J. Lin, Valence conversion and site reconstruction in near-infrared-emitting chromium-activated garnet for simultaneous enhancement of quantum efficiency and thermal stability, *Light: Sci. Appl.*, 2023, **12**, 248.

45 S. W. Yuan, F. G. Wu, J. Wang, L. L. Lou, S. Zhao, D. Y. Zhu and Z. F. Mu, Ultra-broadband near infrared phosphor with wide spectral range and long peak wavelength achieved by double-site occupation, *J. Rare Earths*, 2023, **41**, 1670–1677.

46 S. Guo, L. Ma, M. Abudureyimu, R. Wei, F. Lu, F. Hu and H. Guo, Improving and broadening luminescence in $Gd_{2-x}Al_xGaSbO_7$:Cr^{3+} phosphors for NIR LED applications, *Inorg. Chem. Front.*, 2023, **10**, 2197–2205.

